preprint engrXiv manuscript No.
(will be inserted by the editor)

Evolution of Microstructures on Stainless Steel induced by Ultra-Short Laser Ablation

Norbert Ackerl · Gabriela Fisch · Janko Auerswald · Konrad Wegener

Received: date / Accepted: date

Abstract Ultra-short pulsed laser ablation of stainless steel is accompanied by the evolution of different microstructures. Depending on the fluence, accumulated energy and number of laser passes cones from impurities, laser induced periodic surface structures and cone-like protrusion (CLP) evolve at the surface. These often unwanted morphologies can be inhibited by carefully choosing the strategy and laser parameters. Here, the identified region shows a small processing window for defined 515 nm sub 1 ps ablation leading to low surface roughness. CLP are still not well understood and here a pre-cursor structure is reported. Subsequently, the CLP growth is grain orientation and polarization dependent and studied in more depth. Preferentially, CLP start to evolve at the (101) grain orientations with linear polarized laser radiation. Moreover, a nanoindentation study reveals robust mechanical properties, which could be beneficial for tribology applications in the dynamic regime.

Keywords Laser machining · Self-assembled structures · Cone-like protrusions · Laser induced periodic surface structures · Ultra-short laser pulses · Orthogonal processing · Nanoindentation · Tribology

1 Introduction

In recent years ultra-short pulsed laser machining is becoming a viable technology for industrial application. The equipment costs have been constantly decreasing and several benefits are leading to a strong increase in usage. Having the option to precisely distribute pulses of energy into the material gives a vast number of application. Additionally, the high power density allows to ablate and modify otherwise hard-to-machine materials like ceramics and diamond as well as synthetic or natural composite materials such as carbon fiber re-inforced polymers or mother-of-pearl. Moreover, laser machining can bridge the gap between conventional manufacturing techniques like drilling, milling, electric-discharge machining and semi-conductor technology with the power to span from sub micrometer precision over several 100s of millimeter.

Laser micromaching of stainless steel is of high interest for such applications as e.g. watch dials, hands, appliques, housings, wrist bands or mechanical parts in watch industry, functionalized surface structures for large scale automotive applications, and corrosion resistant markings in the medical industry. However, different microstructures like cones, laser induced periodic surface structures (LIPSS) and cone-like protrusion (CLP) arise depending on the laser parameters [1]. In literature the origins of cones have been identified as slag inclusions from the steel production process, which are primarily Al_2O_3 and MgO [2]. Depending on the steel quality the number of cones near the threshold fluence strongly increases. In parallel LIPSS of low spatial frequency are generated, if linear polarized light is used [3]. Increasing the fluence leads subsequently to the growth of thermal LIPSS, which are perpendicular to the former ones, originating from heat accumulation [4]. Hitherto, there are different regimes of ablation where heat accumulation and local power density is the driving force limiting a high-speed ablation process [5]. However, the CLP structure is not observed after single-pass laser ablation and multiple layers of ablation are necessary [6]. A dependence of local fluence and surface

N. Ackerl · G. Fisch · K. Wegener
Institute of Machine Tools and Manufacturing (IWF), ETH Zurich, Leonhardstrasse 21, 8092 Zurich, Switzerland
J. Auerswald
V-ZUG AG, Industriestrasse 66, 6302 Zug, Switzerland.

speed of the laser leading to precursor structures on the specimen is reported within this contribution.

Defined ablation conditions are a prerequisite for low roughness and efficient laser ablation [7]. In principle the fluence, laser repetition rate, and scan speed are interdependent [8] and no global optimum can be reached. However, depending on the desired process either high material removal rate or surface quality can be reached for $2.5D$ orthogonal strategies. This leads to limiting constraints, where high average power must be distributed on the workpiece by high scan-speeds and repetition rates [9]. To date there is plenty of laser power with high repetition rates available, but depending on the necessary focal spot size the beam steering [10] or controllers [11] are constraining the maximal laser machining speed. Using the laser in a burst mode with small temporal pulse spacing can enhance the maximal applicable average power [12] and ablation rate [13–15]. However, the use of sub-nanosecond spaced ultra-short pulses is still a matter of controversy, where the enhanced efficiency could not be observed [16]. Additionally, the laser energy can be distributed on rotational workpieces by a spindle axis, where one more degree of freedom in terms of processing strategy can be utilized [17,18]. Quasi-tangential laser machining has a huge potential and could utilize the high power nowadays available for ablation , but with increased complexity in the laser path and hatch calculation [19].

Microstructures are not necessarily an unwanted side effect, but can be used to alter the physical interplay at the surface of different materials. Well-known examples are the change in wettability [20,21], optical [22] and tribological properties [23–25]. The idea proposed in this manuscript is to utilize CLP structures for tribology application with high relative surface speed to reach the hydrodynamic lubrication regime. A nanoindentation study on cross-sections of CLP reveals reasonable mechanical properties, with 1:1 aspect ratio in the regime of several micrometers, potentially applicable to lower the coefficient of friction.

2 Experimental techniques

2.1 Material

All studies were carried out on austenitic stainless steel samples of different quality listed in table 1. The composition is allowed to vary in the given range, where every batch can be slightly different. Steel 1.4310 exhibits a higher carbon content than the widest used austenitic stainless steel 1.4301, resulting in higher mechanical strength desired in certain applications but also in slightly lower corrosion resistance. 1.4404 contains more molybdenum and nickel making it more resistant against acids and saline chloride solutions, e.g. human sweat. For the parameter variation a standard Cr/Ni stainless steel 1.4301 with 50 mm^2 and 2 mm thickness served as substrate. The ablation characteristic was studied on the as received state without further sample preparation.

Table 1 Different types of stainless steel inspected, where the percentage in weight of the adjacent species is given and iron fills the gap to 100 %.

classification	1.4310 AISI301	1.4301 AISI304	1.4404 AISI316L
carbon	0.05 - 0.15	≤ 0.07	≤ 0.03
chromium	16.0 - 19.0	17.0 - 19.5	16.5 - 18.5
nickel	6.0 - 9.5	8.0 - 10.5	10.0 - 13.0
molybdenum	0.0 - 0.8	0	2.0 - 3.0
silicon	≤ 2	≤ 1	≤ 1
manganese	≤ 2	≤ 2	≤ 2
grain size	2.5 µm	8 µm	35 µm

The small grain size of these materials makes the study of grain dependencies on laser ablation challenging. Therefore, an additive manufactured 1.4404 austenitic steel cube produced by selective laser melting (SLM) has been used [26]. Due to the powder bed fusion technique with the well controlled energy and temperature gradient larger or similar oriented small grains larger than 30 µm are formed. These grains are elongated in build-up direction, which allows studying the evolution of CLP on the top and side flank of the cube. Here, the specimen was grinded to grit 4000 with SiC sandpaper and following polished with Al_2O_3 suspension with 50 nm to a mirror-like surface.

2.2 Laser machine testbed

Figure 1a shows the table-top experimental setup constituted by a free path beam delivery and a combination of optical and mechanical axes. An Amphos 200 laser with MOPA configuration, YB:YAG Innoslab amplification, and a second harmonic unit serves as source. The fundamental 1030 nm have a pulse duration of about 1 ps, which leads after frequency doubling and the nonlinearity to pulses of 0.8 ps at 515 nm. The used Amphos laser enables a wide parameter variation in terms of average power up to 120 W with green light, repetition rate from single shot up to 40 MHz, however in this study we kept the repetition rate at800 kHz . Moreover, the compressor grating after the Innoslab allows to vary the pulse duration up to 10 ps. The laser radiation is coupled into a galvo scanner, where the raw

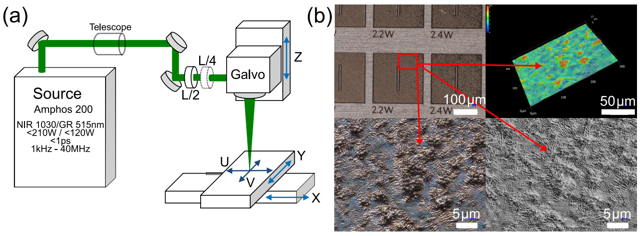

Fig. 1 Laser test bed with mechanical (XYZ) and Galvo (UV) axes for defined positioning (a). Pockets with altered polarization, feed rate and power (b) enables the assessment ablation depth, taper angle, and evolved structures.

beam size is controlled by a Galilean telescope and polarization set by zero-order wave plates. A suction unit with a directional airflow of $250\,\mathrm{m^3\,h^{-1}}$ removes part of the the ablation debris.

2.3 Laser ablation strategy

For the extended parameter study pockets are ablated with a $2.5D$ strategy and rotating 15 adjacent layers by 23 deg per pocket. The geometry is $2\,\mathrm{mm}^2$ with a centered unablated region of 1 mm height 100 µm width to analyze the total ablation, taper flank angle, and edge precision of the laser process. Process parameters varied are the average power from 0.2 W to 2.8 W, feed rate between $100\,\mathrm{mm\,s^{-1}}$ to $1.6\,\mathrm{m\,s^{-1}}$, and the hatch line distance between 1 µm and 5 µm. This leads to a total of 224 parameter fields per hatching distance, where the parameters are chosen to cover the evolution of cones, LIPSS, thermal ripples, and partial to full coverage of the pocket with CLP structures. Moreover, the dependence on the microstructural evolution on polarization state is attained by using half- and quarter-wave plate to adjust and switch the polarization from linear to circular polarization in the focal plane.

2.4 Analysis methods

The pockets are analyzed per set of parameters with optical microscopy using two Keyence devices. By the focus shifting technique of the Keyence VH-X6000 the microstructure is analyzed, depicted in figure 1b. Smaller structures are qualitatively assessed by scanning electron microscopy (SEM) using a Hitachi SU-70. The electron back scattered diffraction (EBSD) study was carried out on a FEI Quanta device. Confocal microscopy using a Keyence VK-X1000 device with blue laser allows to determine the ablation depth in an automated manner.

To assess the modified region by the laser process, cross-sections are created by cutting, grinding and polishing. Beside an optical inspection of the interface region, nanoindentation reveals the mechanical properties. A Nanomechanics iNano with the continuous dynamic oscillation (CSM) method allows to determine the surface near mechanical properties. This technique oscillates the indenter with a sinusoidal driving force, here 110 Hz, and measures force plus displacement with high resolution [27]. The force and indentation depth was calibrated to measure bulk properties and not just the surface near oxide layer [28]. This allowed a indentation distance of 2 µm, which is a distance of three times the indentation depth to avoid impact of neighboring indents. The CSM measurement allows to calculate the materials hardness and elastic modulus for each indent, revealing the spatial distribution of mechanical properties.

3 Results and discussion

3.1 Microstructural evolution

Upon the ablation of steel distinct structures are observed and figure 2 gives an overview of three kinds. Cones, shown in figure 2a, appear after ablating several layers near the threshold fluence and origin from MgO and Al_2O_3 inclusions from the steel production. Due to the higher threshold fluence compared to metals the oxides are ablated less forming a cone structure. In parallel LIPSS with low and high spatial frequency appear in case of linear polarized laser light. Increasing the energy density leads to the formation of thermal ripples, which could be superimposed to the LIPSS depicted in figure 2b. These structural entities can be even formed in a single pass laser process with slow scanning speed and small hatching distance. However, at even higher fluence cone-like protrusions emerge after several layers of ablation, growing with each layer on precursor ripples observable in figure 2c. The micrograph in 2c shows the CLP structure in black and grayish ripples on distinct grains of the SLM additively

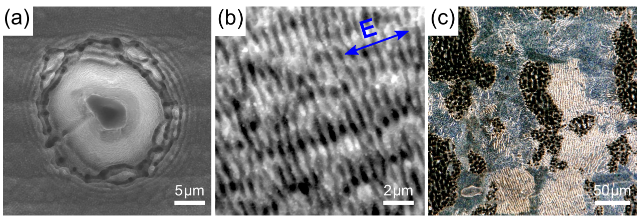

Fig. 2 Inclusions with higher threshold fluence lead to cones (a). Near the threshold LIPSS are observed (b) and at higher fluence and after multi-layer ablation CLP structure evolve, preferentially at precursor structures (c).

manufactured stainless steel sample. Here, the sample was etched for 2 min with V2A to reveal the grains and observe preferential growth on certain orientations. The graph is after ablating 10 layers at $2\,\mathrm{J\,cm^{-2}}$ with a scan speed of $500\,\mathrm{mm\,s^{-1}}$. Interestingly, this ripple structure serves as precursor to the CLP growth and it is assumed that the reflectivity and, therefore, energy coupling to the material is altered. This leads to higher absorbance, which melts a small surface near region even by using ultra-short pulses of less than 1 ps. With each subsequent pass of the laser both structures grow and at after a certain amount of layers the surface is covered with CLP. Figure 3 reveals the dependence of the microstructural evolution on fluence and scan speed after ablating 15 layers with the introduced 2.5D strategy. The contour plot points to a saturation

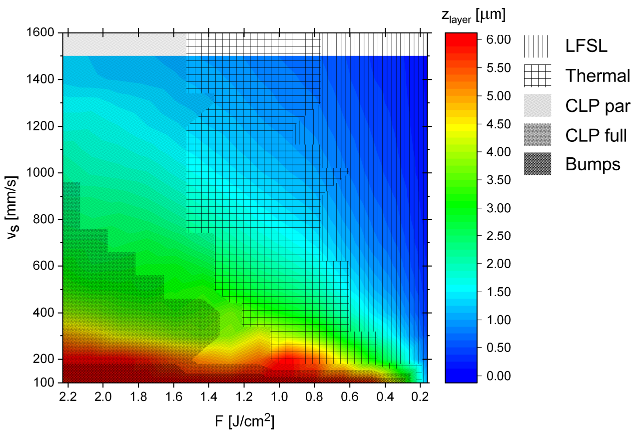

Fig. 3 Layer depth and microstructures observed in dependence of fluence and feed rate after removing 15 layers with linear polarization. A transition from bumps, cones, LIPSS, thermal ripples, and CLP on laser process parameters is revealed.

in terms of material removal rate and layer depth Z_{layer} in good agreement with proposed models in literature [7,9]. At low feed rates starting from moderate fluence of $0.3\,\mathrm{J\,cm^{-2}}$ a bumpy structure due to heat impact is formed, where even semi-spherical structures can be observed. The structures evolve in certain regimes of feed rate, hatch distance and fluence, where figure 3 shows the mapping over a wide field. If the hatching distance is varied the whole dependency is shifted with comparable tendency. If a certain microstructure is desired, a set of parameter can be chosen from this plot or a certain structure prevented. The LIPSS structure can be inhibited by the use of circular polarized light, which additionally has a strong impact on the precursor ripple formation and following CLP coverage of the surface.

3.2 Impact of grain orientation and polarization

To further assess the growth dependencies of CLP structures EBSD mapping was carried out on the SLM sample prior laser ablation. Subsequent stop-motion optical imaging after each ablated layer with $1\,\mathrm{m\,s^{-1}}$ and 2 W reveals the temporal evolution of the microstructures. Figure 4a shows the surface after ablating 17 layers. Clearly, on the (101) orientated grains shown in figure 4b the surface morphology differs observed in a changed reflectivity in the micrograph. These are the ripple precursor structures shown in figure 2c and with each subsequent layer CLP start to grow randomly on exactly these regions. In total 80 layers have been subsequently removed and the final surface is superimposed with the EBSD map in figure 4c. The CLP structure

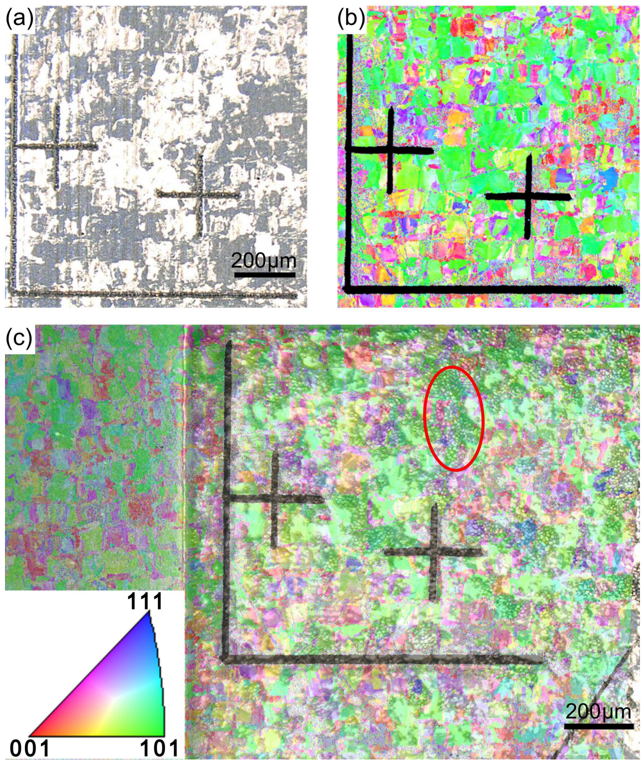

Fig. 4 Optical micro-graph after 17 layer ablated with circular polarization (a) and EBSD from the pristine polished marked surface (b). In (c) an overlay of EBSD measurement after 80 layers show the preferential evolution of CLP at (101) grains, e.g. marked by the red circle.

evolves preferential on the (101) directions, however some structures are observed at different orientation. This is dedicated to underlying grains with the preferred orientation after removing 80 layers and approximately 150 µm of material. The preferred growth at the (101) grains presumably is connected to the packing of the crystal and changes the coupling with the incident electromagnetic wave. A slight change in the thermal conductivity in different orientation of the grains could lead to an accumulation of heat and following thermal ripple formation. However, if this is true the growth and appearance should depend on the grain size, which was not observed within this study. A strong dependence on polarization direction is observed after ablating 160 layer at keeping the parameters unchanged, except the polarization state. Figure 5 clearly reveals a strong dependence, where the surface is almost completely covered for linear polarization in contrast to circular one. This strong dependence on polarization direction tentatively is correlated with the LIPSS formation, which enhances the energy coupling and following thermal ripple creation. A preferred generation of LIPSS starting at defects and discontinuities affecting the surface plasmon polariton, e.g. grain boundaries, could explain the faster growth rate of precursor and CLP. Moreover, even at circular polarization a grain boundary could lead to LIPSS generation matching the defect and polarization direction at a certain point. This is more unlikely and therefore the evolution of LIPSS, ripples and subsequent CLP lessened. However, this still has to be proven by stop-motion imaging in a SEM to resolve the evolution of the smaller structures.

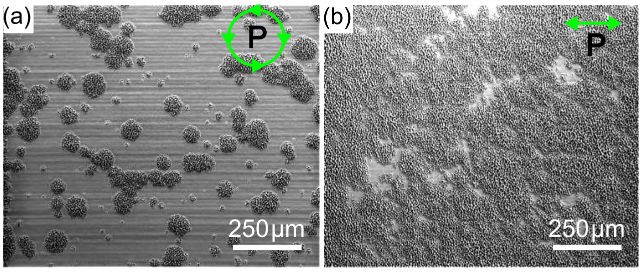

Fig. 5 Polarization dependency using circular (a) and linear (b) polarization on CLP evolution after 160 layer at $2.5\,\mathrm{m\,s^{-1}}$ at $3\,\mathrm{J\,cm^{-2}}$.

3.3 Structure and mechanical properties of CLP

A cross-sectional view on the CLP covered surface in figure 6a shows the evolved protrusions. The structure peaks and valleys are higher and deeper than the samples surface, tentatively formed by surface-near melting and fast resolidification forming different sized CLP depending on the exact dynamics, compare figure 6b. A dependence on scanning speed, local fluence and total accumulated energy from literature [1] corroborates this interpretation. The grain size of the CLP is still under investigations, where edge charging inhibited a straight forward measurement. However, the pseudo-periodic structures appear homogeneously over the whole surface. This could be taken as an approach for generating microstructures for application in e.g. changing the wettability and/or tribology. For exploitation of the potential the mechanical stability plays a role in endurance of the functionality on the surface. Therefore, a nanoindentation study was carried out with an indentation depth of about 100 nm and a distance of 2 µm over a $10\,000\,\mu\mathrm{m}^2$. Using the CSM method the stiffness of the sample is measured, which can be used to calculate hardness and E-modulus. Nanoindentation revealed a small affected zone at the interface with reduced stiffness, see figure 7, where as well free standing cone-like structures could interfere with the measurement. However, the calculation of the bulk regime points to a

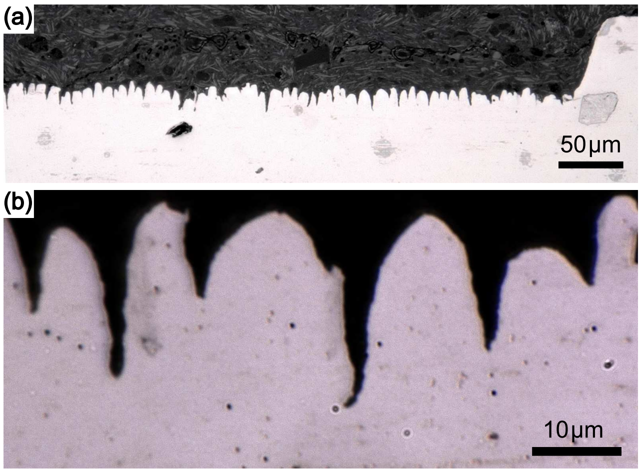

Fig. 6 Cross-section of the CLP structure revealing the size and shape (a). A magnified micrograph shows the CLP width and height in more detail (b).

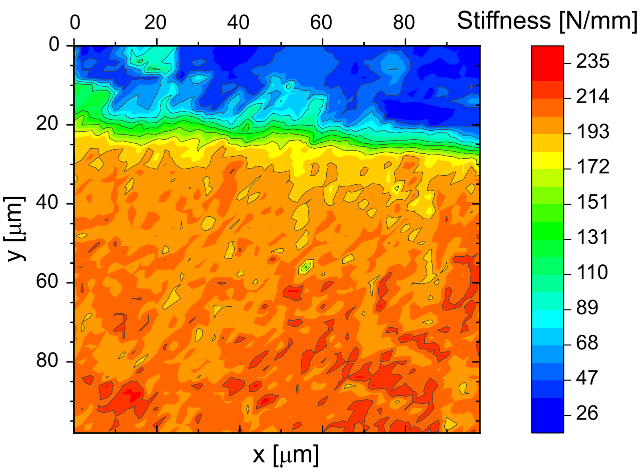

Fig. 7 Nanoindentation with the CSM method allows to measure the mechanical properties, indicating a small change in the surface near region to the embedding material to the bulk.

Young modulus of 160 GPa in good agreement with literature and at the interface to the embedding material to 120 GPa, which corresponds to the green region in figure 7. The overall mechanical properties of the surface near region enable a potential use for tribological application. Dimples and microstructures are known to reduce the coefficient of friction for wet lubricant applications with higher surface speeds. Therefore, the CLP could be used in the hydrodynamic regime with fast surface speed, where the protrusions act as reservoirs to attain a well spread film. However, this has to be studied in more detail and a preliminary test by a pin on disc measurements gathering the Stribeck curves up to several m/s surface speed pointed int the right direction. Nevertheless, a pin diameter with 4 mm and a normal force of 1 N was used, which lead to fast wear on the structures. A fresh study with higher pin diameter and less force will reveal the potential for tribological applications.

4 Conclusion and Outlook

Ultra-short pulsed laser ablation on stainless steel reveals self-organized microstructures, which are dependent on the laser and process parameter. A regime for defined ablation without cones and CLP has been identified, where LIPSS can be mitigated by circular polarization. The CLP start to grow succeeding at least one ablated layer on ripple precursor structures. With each layer the CLP and ripple structure cover more surface area ending in full coverage. These two structures preferentially assemble at the (101) direction of the face-centered cubic austenitic steel grains under investigation. Moreover, a strong dependence on the laser polarization direction is reported. The CLP geometry can be changed by laser parameters, where the resolidification of the surface molten layer plays the crucial role.

Nanoindentation pointed to a slight change in stiffness compared to the bulk properties with an E-modulus of about 120 GPa at the interface. Potentially, CLP structures are a viable candidates for tribological application to reduce friction and wear via laser surface structuring. A preliminary study pointed to a reduced coefficient of friction in the hydrodynamic regime of lubrication.

Acknowledgments

The authors want to thank the Swiss National Fund (FuSSiT/169654) for funding. Thanks to Keyence Switzerland and, especially, Martin Banzer for support and the possibility to implement a Keyence VH-X6000 temporarily in our laboratories. Moreover, N.A. wants to acknowledge Reto Völlmin from Keyence Switzerland for support with the confocal Keyence VK-X1000 and setting up the automated measurement routines. The help of Marianna Diamantopoulou with the EBSD studies is highly appreciated. Special thanks from N.A. to Peter Hosemann at UC Berkeley for hosting during the conception and writing of this manuscript.

References

1. V. Villerius, H. Kooiker, J. Post, Y. Pei, Int. J. Mach. Tools Manuf. **138**(October 2018), 27 (2019). DOI 10.1016/j.ijmachtools.2018.11.003
2. E.J.Y. Ling, J. Saïd, N. Brodusch, R. Gauvin, P. Servio, A.m. Kietzig, Appl. Surf. Sci. **353**, 512 (2015). DOI 10.1016/j.apsusc.2015.06.137
3. S. Faas, U. Bielke, R. Weber, T. Graf, Appl. Phys. A **124**(9), 612 (2018). DOI 10.1007/s00339-018-2040-4
4. P. Mannion, J. Magee, E. Coyne, G. O'Connor, T. Glynn, Appl. Surf. Sci. **233**(1-4), 275 (2004). DOI 10.1016/j.apsusc.2004.03.229
5. A. Gillner, J. Finger, P. Gretzki, M. Niessen, T. Bartels, M. Reininghaus, J. Laser Micro/Nanoengineering **14**(2) (2019). DOI 10.2961/jlmn.2019.02.0003
6. E.J.Y. Ling, J. Saïd, N. Brodusch, R. Gauvin, P. Servio, A.M. Kietzig, Appl. Surf. Sci. **353**, 512 (2015). DOI 10.1016/j.apsusc.2015.06.137
7. A. Žemaitis, M. Gaidys, M. Brikas, P. Gečys, G. Račiukaitis, M. Gedvilas, Sci. Rep. **8**(1), 1 (2018). DOI 10.1038/s41598-018-35604-z
8. N. Ackerl, M. Warhanek, J. Gysel, K. Wegener, J. Eur. Ceram. Soc. **39**(4), 1635 (2019). DOI 10.1016/j.jeurceramsoc.2018.11.007
9. B. Neuenschwander, B. Jäggi, M. Schmid, G. Hennig, Phys. Procedia **56**, 1047 (2014). DOI 10.1016/j.phpro.2014.08.017
10. B. Jäggi, B. Neuenschwander, M. Zimmermann, M. Zecherle, E.W. Boeckler, (2016), vol. 973513, p. 973513. DOI 10.1117/12.2210791
11. N. Ackerl, P. Boerner, K. Wegener, J. Laser Appl. **31**(2), 022501 (2019). DOI 10.2351/1.5096079
12. B. Jäggi, D.J. Förster, R. Weber, B. Neuenschwander, Adv. Opt. Technol. **7**(3), 175 (2018). DOI 10.1515/aot-2018-0003
13. B. Jäggi, S. Remund, Y. Zhang, T. Kramer, B. Neuenschwander, J. Laser Micro/Nanoengineering **12**(3), 258 (2017). DOI 10.2961/jlmn.2017.03.0015
14. C. Gaudiuso, G. Giannuzzi, A. Volpe, P.M. Lugarà, I. Choquet, A. Ancona, Opt. Express **26**(4), 3801 (2018). DOI 10.1364/OE.26.003801
15. G. Bonamis, K. Mishchick, E. Audouard, C. Hönninger, E. Mottay, J. Lopez, I. Manek-Hönninger, J. Laser Appl. **31**(2), 022205 (2019). DOI 10.2351/1.5096087
16. J. Mur, R. Petkovšek, Appl. Surf. Sci. **478**(December 2018), 355 (2019). DOI 10.1016/j.apsusc.2019.01.182
17. N. Ackerl, M. Warhanek, J. Gysel, K. Wegener, engrXiv Prepr. p. 22 (2019). DOI 10.31224/osf.io/cnm35
18. M. Warhanek, J. Mayr, C. Dörig, K. Wegener, Lasers Manuf. Mater. Process. **4**(4), 193 (2017). DOI 10.1007/s40516-017-0046-y

19. N. Ackerl, M. Warhanek, J. Gysel, K. Wegener, Int. J. Adv. Manuf. Technol. **103**(1-4), 1105 (2019). DOI 10.1007/s00170-019-03540-5
20. R. Lloyd, A. Abdolvand, M. Schmidt, P. Crouse, D. Whitehead, Z. Liu, L. Li, Appl. Phys. A Mater. Sci. Process. **93**(1), 117 (2008). DOI 10.1007/s00339-008-4646-4
21. C.S. Sharma, C. Stamatopoulos, R. Suter, P.R. von Rohr, D. Poulikakos, ACS Appl. Mater. Interfaces p. acsami.8b09067 (2018). DOI 10.1021/acsami.8b09067
22. E.I. Ageev, V.P. Veiko, E.A. Vlasova, Y.Y. Karlagina, A. Krivonosov, M.K. Moskvin, G.V. Odintsova, V.E. Pshenichnov, V.V. Romanov, R.M. Yatsuk, Opt. Express **26**(2), 2117 (2018). DOI 10.1364/OE.26.002117
23. M.R. Ripoll, R. Simič, J. Brenner, B. Podgornik, Tribol. Lett. **51**(2), 261 (2013). DOI 10.1007/s11249-013-0170-6
24. J. Bonse, R. Koter, M. Hartelt, D. Spaltmann, S. Pentzien, S. Höhm, A. Rosenfeld, J. Krüger, Appl. Surf. Sci. **336**, 21 (2015). DOI 10.1016/j.apsusc.2014.08.111
25. J. Bonse, S. Kirner, M. Griepentrog, D. Spaltmann, J. Krüger, Materials (Basel). **11**(5), 801 (2018). DOI 10.3390/ma11050801
26. T. Heeling, K. Wegener, Addit. Manuf. **22**(February), 334 (2018). DOI 10.1016/j.addma.2018.05.026
27. X. Li, B. Bhushan, Mater. Charact. **48**(1), 11 (2002). DOI 10.1016/S1044-5803(02)00192-4
28. P. Hosemann, Scr. Mater. **143**, 161 (2018). DOI 10.1016/j.scriptamat.2017.04.026